




Ethanol steam reforming: understanding changes in the activity and stability of Rh/M_xO_y catalysts as function of the support

Thenner S. Rodrigues^{1,2,*} , Felipe A. e Silva^{1,2}, Eduardo G. Candido¹, Anderson G. M. da Silva³, Rafael dos S. Geonmonond³, Pedro H. C. Camargo³, Marcelo Linardi¹, and Fabio C. Fonseca¹

¹Instituto de Pesquisas Energéticas e Nucleares, IPEN-CNEN/SP, Av. Prof. Lineu Prestes, 2242, São Paulo, SP 05508-000, Brazil

²Nanotechnology Engineering Program, Alberto Luiz Coimbra Institute for Graduate Studies and Research in Engineering, COPPE, Federal University of Rio de Janeiro, Av. Horácio Macedo, 2030, Rio de Janeiro, RJ 21941-972, Brazil

³Departamento de Química Fundamental, Instituto de Química, Universidade de São Paulo, Av. Prof. Lineu Prestes, 748, São Paulo, SP 05508-000, Brazil

Received: 18 December 2018

Accepted: 26 April 2019

Published online:

28 May 2019

© Springer Science+Business Media, LLC, part of Springer Nature 2019

ABSTRACT

We reported herein a systematic investigation on how the nature of the support affected the catalytic performances of Rh nanoparticles. The prepared catalysts were denoted as Rh/M_xO_y, where M corresponded to Ce, Ti, Si, Zn, and Al, and Rh was Rh³⁺ reduction to Rh nanoparticles on the surface of oxides. This strategy was performed in a single step using urea as a mediator and in the absence of any other stabilizer or capping agent. The Rh nanoparticles displayed relatively similar sizes, shapes, and uniform distribution over the supports, differing only in terms of the nature of the support. This strongly affected the metal–support interaction between Rh nanoparticles and the respective oxides, leading to significant differences in their catalytic performances toward the ethanol steam reforming. Here, not only the catalytic activity (in terms of ethanol conversion) was affected, but both the selectivity and stability were also influenced by the nature of the oxide support. Interestingly, the reaction paths as well as the deactivation profile were completely changed as function of the employed support. Such differences were associated with differences in the oxygen storage, oxygen mobility, and acidity/basicity of the supports. We believe that our results can contribute to the development and understanding of Rh-supported catalysts for the applications toward gas-phase transformations such as the ethanol steam reforming reaction.

Address correspondence to E-mail: thenner@pent.coppe.ufrj.br

Introduction

Ethanol steam reforming is an important chemical transformation that makes possible the conversion of a renewable liquid raw material to hydrogen (H_2) in the presence of water (H_2O), having carbon dioxide (CO_2) as a coproduct [1–4]. However, under real experimental conditions, not only stoichiometric H_2 and CO_2 are obtained as products, but a relatively complex reaction mixture containing compounds formed by a variety of parallel reactions that can also take place, including ethanol dehydrogenation, dehydration, and decomposition, coke deposition, among others [5, 6]. Nevertheless, a variety of previous work has shown that the selectivity can be controlled/optimized in order to direct the reaction process for the maximum of H_2 production. In this context, the main strategies used to improve the performance of ethanol vapor reforming system include the systematic manipulation of process parameters such as temperature, stoichiometry of the reagents and/or their feeding flows, and gas hourly space velocity (GSHV) [1–3, 5–8]. Moreover, the synthesis of supported nanocatalysts has evolved into an important strategy for the development of increasingly efficient ethanol steam reforming processes [6, 9–13].

Typically, the structure of supported nanocatalysts for catalysis is described by the active phase and the solid support. The active phase is usually based on noble metal nanoparticles such as Au [14], Pd [15], Pt [16], Rh [17, 18], Ru [19], and among others, having higher activity, selectivity, and resistance against deactivation. Non-noble metals such as Ni and Co [6, 9, 20] have also been employed, which are more accessible, with great potential for reforming, but they are not so active, selective, and stable and tend to deactivate in short times of reaction. On the other hand, the solid support represents much more than only a carrier or disperser of the active phase. Some previous studies have shown that the support, according to their chemical nature, can effectively enhance the catalytic activity and manipulate the reaction pathways for desired reactions and prevent the deposition of carbon-based compounds that tends to deactivate the catalyst [8, 9, 13, 21–25].

In order to produce supported nanocatalysts, two main strategies are usually employed. The first is the synthesis of nanoparticles and their further

incorporation over the surface of solid supports after steps of purification that include washing and centrifugation or filtration [26–31]. This method is extremely interesting due to the possibility of the precise control over the properties that defined the nanoparticles (size, shape, structure, composition, etc.) and the amount of metal loaded in respective nanocatalyst. However, some issues in this strategy can also be pointed such as the need for two or more steps of synthesis, limitation of scale in the synthesis of the nanoparticles, difficulty in the purification, loss of nanoparticles during washing, and the presence of organic and inorganic compounds usually employed in the synthesis of the desired nanoparticles [26–31]. The second strategy consists in the synthesis of nanoparticles in the presence of support as a physical template for deposition, which implies in the formation/growth of the respective nanoparticles on the surface of the support on which it ends up depositing on it [32–34]. In this strategy, the main limitations are the poor control over the properties of the nanoparticles and the amount of metal loaded onto the supports (depending on the affinity between metal and support). However, this procedure can be performed in a single step and the purification and washing steps are easier, can be performed in the absence of organic compounds (templates, stabilizers, capping agents, etc.), and provide catalysts with enhanced metal–support interactions which tends maximize their activities and prevent against agglomeration and metal loss during purification and catalytic experiments [32–37].

In this paper, we describe a systematic investigation on how the nature of the support affects the overall performance of Rh/M_xO_y catalysts (where $M = Ce, Ti, Si, Zn, \text{ and } Al$) toward ethanol steam reforming. To this end, we firstly employed an urea-assisted deposition protocol, which was responsible for Rh^{3+} reduction to Rh its and further incorporation on commercial oxide supports in the absence of any other stabilizer and/or capping agent. After their synthesis and characterization, the catalytic performance of the Rh/M_xO_y catalysts was investigated toward the ethanol steam reforming, which was chosen as a model reaction due to its importance in the production of hydrogen from a renewable raw material. More specifically, we were particularly interested in investigating how different activity supports would influence the catalytic performance of the nanocatalyst in terms of activity, selectivity,

and stability. We found herein that the nature of the support was imperative in the catalytic behavior toward ethanol steam reforming, in which the activity, selectivity, stability, and deposition of carbon-based compounds were strongly influenced by each employed catalytic support.

Experimental

Materials and instrumentation

Analytical-grade cerium(IV) oxide (CeO_2 , 99.9%, Evonik), silicon(IV) oxide (SiO_2 , 99.9%, Sigma-Aldrich), zinc(II) oxide (ZnO , 99%, CAAL), aluminum(III) oxide (Al_2O_3 , 99%, CAAL), titanium(IV) oxide (TiO_2 , 99%, CAAL), rhodium(III) chloride (RhCl_3 , 99.99%, Sigma-Aldrich), urea ($\text{CH}_4\text{N}_2\text{O}$, 99.75%, Vetec), ethanol ($\text{C}_2\text{H}_6\text{O}$, 99.5%, Sigma-Aldrich), and silicon carbide (SiC , $\geq 97.5\%$, Sigma-Aldrich) were used as received.

Scanning electron microscopy (SEM) images were obtained using a JEOL field emission gun microscope JSM 6330F operated at 5 kV. Samples were prepared by drop-casting an aqueous suspension containing the nanostructures over a silicon wafer, followed by drying under ambient conditions. The high-resolution transmission electron microscopy (HRTEM) images were obtained with a Tecnai FEI G20 microscope operated at 200 kV. Samples for HRTEM were prepared by drop-casting an aqueous suspension of the materials over a carbon-coated copper grid, followed by drying under ambient conditions. The Rh weight percentages were measured by inductively coupled plasma optical emission spectrometry (ICP-OES) using a Spectro Arcos equipment. Specific surface areas were determined by the Brunauer–Emmett–Teller equation (BET method) using a Quantachrome ChemBET Pulsar instrument equipped with a thermal conductivity detector. Typically, 0.05 g of a catalyst was pretreated with He flow at 300 °C for 3 h and then cooled down to room temperature. After this step, the specific surface areas were determined from nitrogen adsorption at -196 °C using liquid nitrogen under atmospheric pressure. Temperature-programmed reduction with hydrogen (H_2 -TPR) and CO chemisorption studies were carried out in the Quantachrome ChemBET Pulsar instrument equipped with a thermal conductivity detector right after a cold trap containing liquid

nitrogen. Typically, 0.05 g of a catalyst was dried with He flow at 200 °C for 20 min and then cooled down to room temperature. The TPR profiles were obtained between 50 and 1100 °C in a flow of 10% H_2/N_2 , the temperature increasing linearly at a rate of 10 °C min^{-1} . The CO chemisorption data and carbon monoxide temperature-programmed desorption profiles (CO-TPD) were carried out on both fresh and spent catalysts. The area of gas-exposed Rh was measured by CO pulse chemisorption at 50 °C using pulses of 5% CO in He. Prior to the chemisorption, 0.05 g of the catalyst was pretreated at 450 °C under a 10% H_2/N_2 flow and the temperature increased linearly at a rate of 10 °C min^{-1} and kept at 450 °C for 1 h, and then cooled down to 50 °C. Sequentially, temperature-programmed desorption was performed by heating in a stream of He at 75 $\text{cm}^3 \text{min}^{-1}$ between 50 and 1100 °C with a heating rate of 10 °C min^{-1} . The X-ray diffraction (XRD) data were obtained using a Rigaku Miniflex II equipment and Cu K-alpha radiation. The diffraction patterns were measured in the range of 20°–90° 2θ with a 1° min^{-1} angular speed scan. Thermogravimetric (TGA) measurements were carried out using a Setaram-LabSys equipment in the range of temperature of 25–1000 °C using a heating rate of 5 °C min^{-1} under synthetic air flow. Before the analyses, the samples were pretreated under vacuum at 25 °C for 1 h. Raman spectra were collected using a Renishaw InVia Reflex coupled to a Leica DM 2500 M microscope and a CCD detector. The laser excitations used were 632.8 nm (He/Ne source), and the objective was a 50 × objective (NA = 0.9).

Synthesis of $\text{Rh}/\text{M}_x\text{O}_y$ (M = Ce, Ti, Si, Zn, and Al) catalysts

The incorporation of Rh onto the commercial supports was performed using a urea-mediated deposition method approach [32, 34]. Typically, 2 g of the respective support, 100 mL of deionized water and 0.616 g of urea were stirred at 70 °C for homogenization. After that, 400 μL of Rh^{3+} aqueous solution 0.25 M was added, and the reaction mixture was stirred at 90 °C for 4 h. After their synthesis, the products were collected by centrifugation and washed five times with water (40 mL) and three times with ethanol (40 mL) by successive rounds of centrifugation and removal of the supernatant. Finally, the resulting products were dried at 120 °C

for 2 h under air and calcined at 500 °C for 2 h with a heating rate of 5 °C min⁻¹.

Catalytic ethanol steam reforming

Catalytic experiments were carried out at atmospheric pressure in a fixed-bed quartz tubular reactor, 5 mm of inner diameter, packed with 1 cm of pure support or 1 cm of catalyst with 0.28 mmol of active metal (Rh) diluted in silicon carbide, if necessary, placed in a vertical oven equipped with a thermocouple in the middle for the control of temperature. Prior to reaction, the catalyst was pre-reduced under hydrogen atmosphere at 450 °C for 1 h under a flow rate of 30 cm³ min⁻¹. With the oven at 550 °C, water and ethanol were fed into the reactor using a system with two saturators to obtain a H₂O/CH₃CH₂OH molar ratio = 3. Nitrogen was used as a carrier gas at a total flow rate of 20 cm³ min⁻¹. Herein, the residence time and gas hourly space velocity corresponded to 0.59 s and 6115 h⁻¹, respectively. The reactants and the reaction products were analyzed by gas chromatograph (Agilent 7890A), equipped with a thermal conductivity detector (TCD) and a flame ionization detector (FID) connected in series.

The catalytic performances were evaluated by the profiles of conversion of ethanol (C_{CH₃CH₂OH}), selectivity for hydrogen (S_{H₂}), and selectivity for the carbon-based products (S_X, where X represents CO₂, CO, CH₄, C₂H₄, CH₃CHO, or CH₃COCH₃) as a function of the reaction time, which were calculated by Eqs. 1–3 as follows [38]:

$$C_{\text{CH}_3\text{CH}_2\text{OH}} (\%) = \frac{(\text{mol}_{\text{CH}_3\text{CH}_2\text{OH}, \text{in}} - \text{mol}_{\text{CH}_3\text{CH}_2\text{OH}, \text{out}})}{\text{mol}_{\text{CH}_3\text{CH}_2\text{OH}, \text{in}}} \times 100 \quad (1)$$

$$S_{\text{H}_2} (\%) = \frac{(\text{mol}_{\text{H}_2}/6)}{(\text{mol}_{\text{CH}_3\text{CH}_2\text{OH}, \text{in}} - \text{mol}_{\text{CH}_3\text{CH}_2\text{OH}, \text{out}})} \times 100 \quad (2)$$

$$S_X (\%) = \frac{\left(\text{mol}_X / \left(\frac{2}{C}\right)\right)}{(\text{mol}_{\text{CH}_3\text{CH}_2\text{OH}, \text{in}} - \text{mol}_{\text{CH}_3\text{CH}_2\text{OH}, \text{out}})} \times 100 \quad (3)$$

Herein, C is the number of carbon atoms in these respective species.

Results and discussion

Our studies started with the synthesis of Rh/M_xO_y (M = Ce, Ti, Si, Zn, and Al) catalysts, which can be described as Rh-based nanoparticles supported over a variety of commercial oxides that include CeO₂, TiO₂, SiO₂, ZnO, and Al₂O₃. Herein, we employed a facile method for the preparation of metal-supported heterogeneous catalysts, in which the deposition-precipitation of Rh nanoparticles is achieved in a single step using urea as reductant [34, 39]. Interestingly, by using this strategy, catalysts displaying cleaner surfaces can be produced after their purification step. The purification consisted of washing with water and ethanol (responsible for removal of residual urea, Cl⁻ ions, and Rh species not adhered to the support) followed by the calcination (responsible for the removal/decomposition of urea adhered to the support), which is extremely desired in the context of heterogeneous catalysis [34]. In this context, to determine the degradation temperature of urea, we performed thermogravimetric analyses under the same conditions of the calcination procedure. As shown in Fig. 1a, pure urea was completely decomposed after 500 °C and no more significant weight loss was observed after this temperature. This behavior was also observed for Rh/CeO₂ catalyst (Fig. 1b), which was selected as the model sample due to its wide use as catalyst in several chemical processes and presented only 0.3% of weight loss after 500 °C. Figure 1d shows the Raman spectrum of the Rh/CeO₂ catalyst after 2 h of calcination at 500 °C under air, and a single peak at 463 cm⁻¹ associated with CeO₂ is observed [40, 41]. Thus, no peaks associated with urea were observed (the Raman spectrum for pure urea is depicted in Fig. 1c for comparison) [42], illustrating its complete degradation/removal under our experimental conditions.

Figure 2 shows the scanning electron microscopy (SEM), energy-dispersive X-ray spectroscopy (SEM-EDX), and high-resolution transmission electron microscopy (HRTEM) images for the Rh/M_xO_y (M = Ce, Ti, Si, Zn, and Al) catalysts: Rh/CeO₂ (Fig. 2a–e), Rh/TiO₂ (Fig. 2f–j), Rh/SiO₂ (Fig. 2k–o), Rh/ZnO (Fig. 2p–t), and Rh/Al₂O₃ (Fig. 2u–y), respectively.

In the first column, we can observe that all Rh/M_xO_y catalysts kept the typical features of their respective commercial solid supports (Figure S1) such as poor control over shape and size, and no

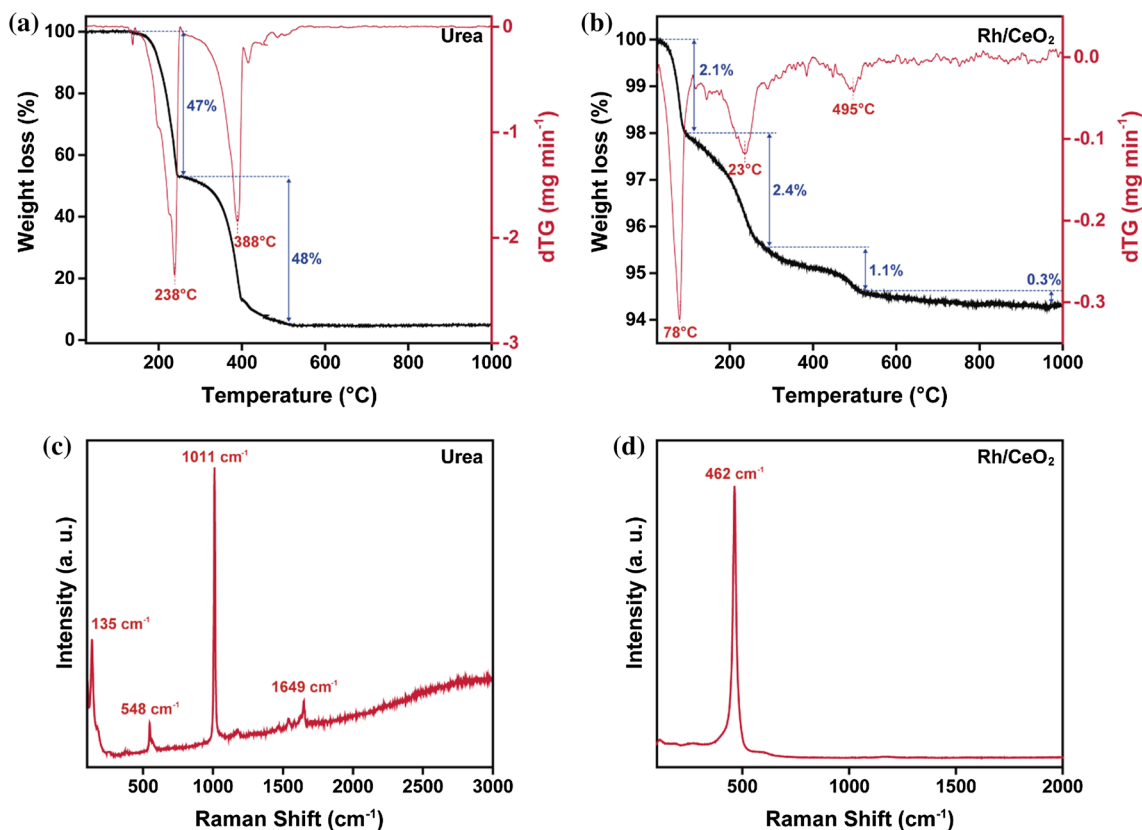


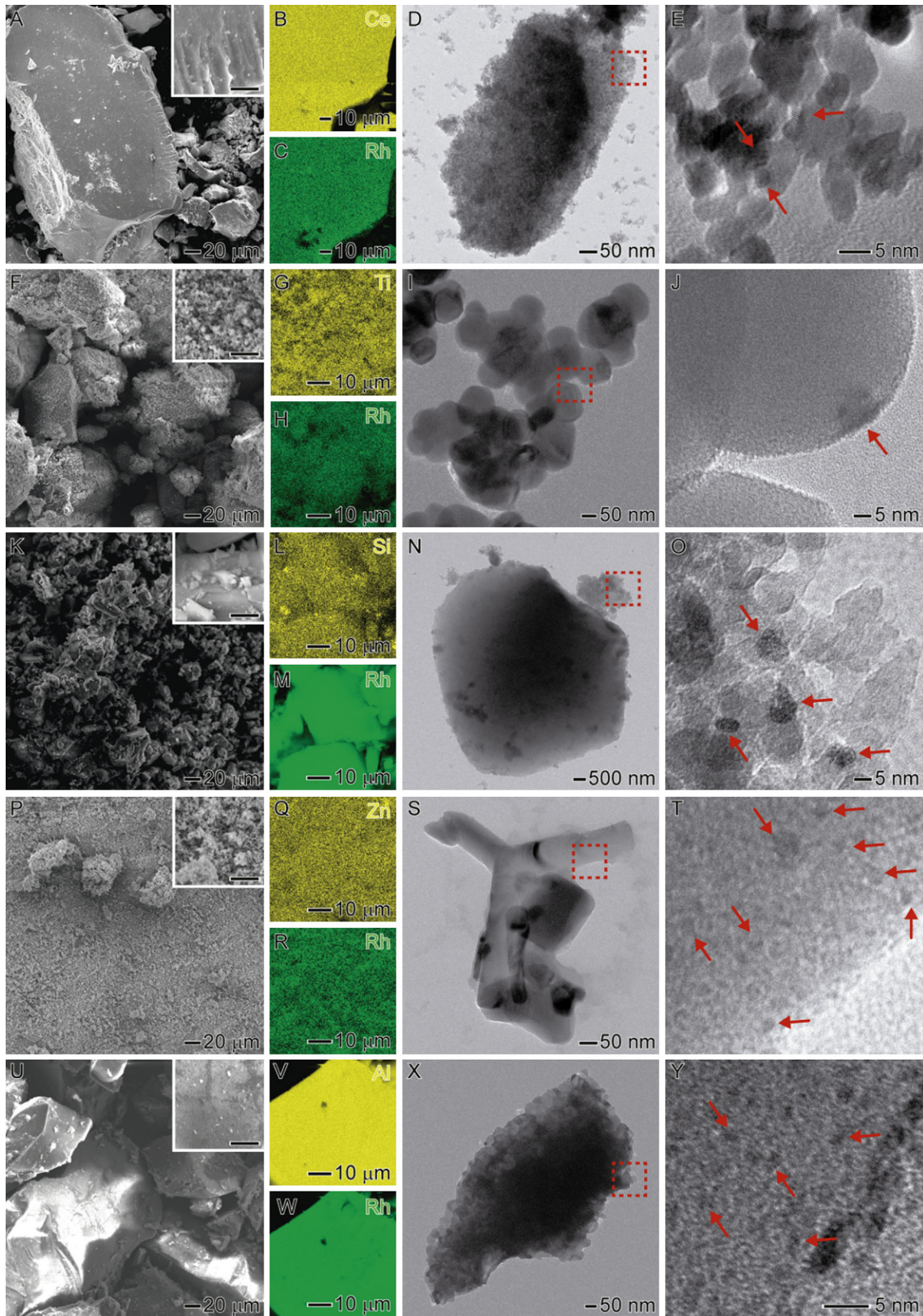
Figure 1 Thermogravimetric analyses of pure urea (a) and Rh/CeO₂ catalyst (b), and Raman spectra of pure urea (c) and d Rh/CeO₂ catalyst.

morphological changes could be detected after Rh deposition, as corroborated by the HRTEM images (third column). On the other hand, as depicted by the low-magnification SEM–EDX images (second column), a homogeneous distribution of the Rh-based nanostructures (green) over the surfaces of all employed supports (yellow) was observed. This behavior is very important in the context of catalytic applications as a better metal distribution usually leads to an increase in the metallic surface area and thus catalytic activities. The fourth column depicts zoom-in images of the areas highlighted in red in the third column. Here, as indicated by the red arrows, due to the less bright mass–thickness contrast we could identify the formation of Rh nanoparticles with sizes corresponding to 2.7 ± 0.4 nm for Rh/CeO₂ (Fig. 2e), 4.8 ± 1.5 nm for Rh/TiO₂ (Fig. 2j), 1.9 ± 0.5 nm for Rh/SiO₂ (Fig. 2o), 4.7 ± 1.1 nm for Rh/ZnO (Fig. 2t), and 2.1 ± 0.3 nm for Rh/Al₂O₃ (Fig. 2y). Figure S2 shows the histograms of size distribution of Rh nanoparticles over all employed oxide supports.

The XRD patterns for the pure commercial oxide support and Rh/M_xO_y catalysts are depicted in Fig. 3. Here, all pure supports (Fig. 3a, left column) presented profiles composed by well-defined peaks assigned to only their crystalline phases without any detected impurities [43–45]. After Rh incorporation, the XRD profiles for the resulting Rh/M_xO_y catalysts (Fig. 3b, right column) remained mostly unchanged suggesting that no destruction/modification of supports was observed after the process, in agreement with the SEM data (Figs. 2 and S1). In addition, no peaks assigned to Rh-based species could be detected, in agreement with their small sizes and low loadings in the samples [46].

Table 1 shows the values of the features for the Rh/M_xO_y catalysts measured by ICP-OES, EDX, N₂ physisorption, and CO chemisorption.

The Rh weight percentages in the Rh/M_xO_y catalysts were determined by ICP-OES analyses and corresponded to 0.023, 0.020, 0.163, 0.476, and 0.040% for Rh/CeO₂, Rh/TiO₂, Rh/SiO₂, Rh/ZnO, and Rh/Al₂O₃, respectively, which were very similar to the



◀ **Figure 2** SEM (first column), SEM–EDX elemental map (second column), and HRTEM (second and third columns) images for the Rh/ M_xO_y catalysts obtained from the urea-assisted Rh deposition method. **a–e** Rh/CeO₂, **f–j** Rh/TiO₂, **k–o** Rh/SiO₂, **p–t** Rh/ZnO, and **u–y** Rh/Al₂O₃ catalysts.

values obtained by chemical analysis by EDX (Figure S3). Even though the same amount of Rh was used for the preparation of all obtained catalysts, we could observe a significant variation in the Rh loading among the samples depending on the oxide

employed as support. This behavior can be associated with the nature of the oxides, which presents different points of zero charge under the same experimental condition. Thus, the interaction of the Rh precursor with the surface of the metal oxides occurs in different magnitudes, and consequently, the level of Rh deposition over their surfaces is affected [47, 48]. The specific surface area for all Rh/ M_xO_y catalysts varied in the range of 4.6–154.5 m² g⁻¹. Here, these differences are associated with the nature of the commercial supports; after Rh incorporation, no significant variation in their surface areas was

Figure 3 XRD patterns for the pure commercial oxide supports **(a)** and Rh/ M_xO_y catalysts **(b)**.

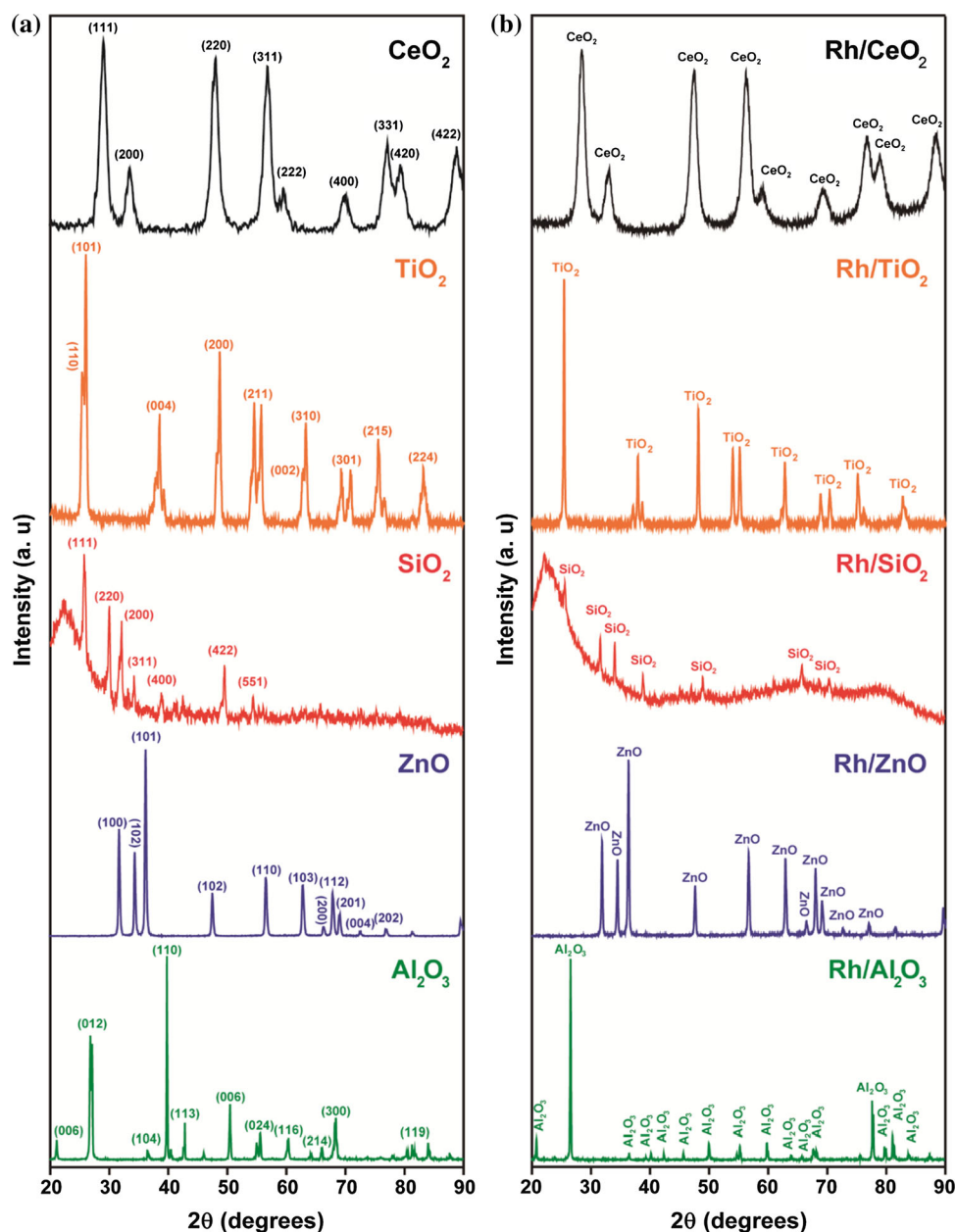


Table 1 Surface properties of the obtained catalysts measured by ICP-OES, N₂ physisorption and CO chemisorption

Sample	Rh content (wt%)	Surface area (m ² g ⁻¹ catalyst)	Metallic area (m ² g ⁻¹ metal)	Rh dispersion (%)
Rh/CeO ₂	0.023 (0.05) ^a	77.4 (85.9) ^b	130.9	29.7
Rh/TiO ₂	0.020 (0.02) ^a	17.9 (19.4) ^b	168.7	38.3
Rh/SiO ₂	0.163 (0.10) ^a	154.5 (164.1) ^b	48.4	11.0
Rh/ZnO	0.476 (0.38) ^a	4.6 (5.6) ^b	105.5	24.0
Rh/Al ₂ O ₃	0.040 (0.05) ^a	14.5 (16.6) ^b	65.7	14.9

^aEDX measurements^bPure support

detected for all obtained Rh/M_xO_y catalysts, showing the robustness of our employed approach for the synthesis of supported catalysts, in agreement with SEM (Figs. 2 and S1) and XRD (Fig. 3) results. The metallic surface area and Rh dispersion were measured by CO chemisorption analyses and decreased as follows: Rh/TiO₂ > Rh/CeO₂ > Rh/ZnO > Rh/Al₂O₃ > Rh/SiO₂. Here, the values for both the metallic surface area and Rh dispersion were relatively higher compared with other reported Rh supported over commercial supports and these superior values are consistent with the small sizes and fine distribution of Rh nanoparticles onto the surface of the commercial oxide supports [25, 49], as observed by SEM–EDX and HRTEM results (Fig. 2).

Figure 4 depicts the H₂-TPR and CO-TPD profiles for all Rh/M_xO_y catalysts. In the profiles for the pure commercial supports (Fig. 4a, first column), we could observe that CeO₂, TiO₂, and SiO₂ presented peaks of H₂ consumption. More specifically, pure CeO₂ presented two peaks centered at 612 and 890 °C assigned to the reduction of surface and bulk cerium oxide species, respectively [50, 51]. TiO₂ presented two intense peaks at 681 and 1008 °C with a shoulder at 810 °C peaks attributed to the reduction of TiO₂ to Ti [52, 53], and pure SiO₂ presented two peaks centered at 803 and 984 °C both assigned to the reduction of SiO₂ phases [29, 53]. In contrast, ZnO and Al₂O₃ showed no peaks of H₂ consumption being stable even after 1100 °C, in agreement with previous reports [54–56]. Herein, different reduction profiles were observed for each employed oxide due to their intrinsic properties such as their reducibility in the presence of H₂ flow. After addition of Rh onto the surface of the commercial oxides, which led to the formation of Rh/M_xO_y catalysts, the reduction peaks associated with the pure supports were shifted to

lower temperatures indicating an increase in their reducibility properties [57]. Moreover, in all cases we could observe peaks centered in the range of 130–615 °C associated with the reduction of Rh-based species to zero-valent Rh [58, 59]. Here, the differences in the temperature of reduction can be associated with the magnitude of the metal–support interaction, which is specific for each employed oxide as support. This hypothesis is reinforced by the CO-TPD profiles (third column), in which the temperature of CO desorption varied as a function of nature of the employed support [60, 61].

After the synthesis and characterization of the Rh/M_xO_y catalysts, we turned our attention to their catalytic evaluation toward the ethanol steam reforming, which is considered one of the most sustainable, green, and renewable routes for hydrogen production [62–64]. Presently, the main limitations in the ethanol steam reforming are the production of heterogeneous catalysts, which can promote high levels of ethanol conversions with high selectivities for hydrogen production and low amounts of carbon-based compounds (which deposit over the structure of the catalysts and tend to decrease their activities) and toxic products as carbon monoxide. Thanks to its recognized performance for ethanol steam reforming, Rh was selected as the active phase of a series of catalysts, in which the catalytic behavior was investigated as a function of nature of the support in terms of activity and selectivity [11, 25, 65].

Figure 5 depicts the ethanol conversion percentages and products selectivities in the presence of Rh/CeO₂ (Fig. 5b), Rh/TiO₂ (Fig. 5c), Rh/SiO₂ (Fig. 5d), Rh/ZnO (Fig. 5e), and Rh/Al₂O₃ (Fig. 5f) catalysts using the H₂O/CH₃CH₂OH molar ratio = 3 (theoretical stoichiometric ratio, Eq. 4) and 550 °C, which

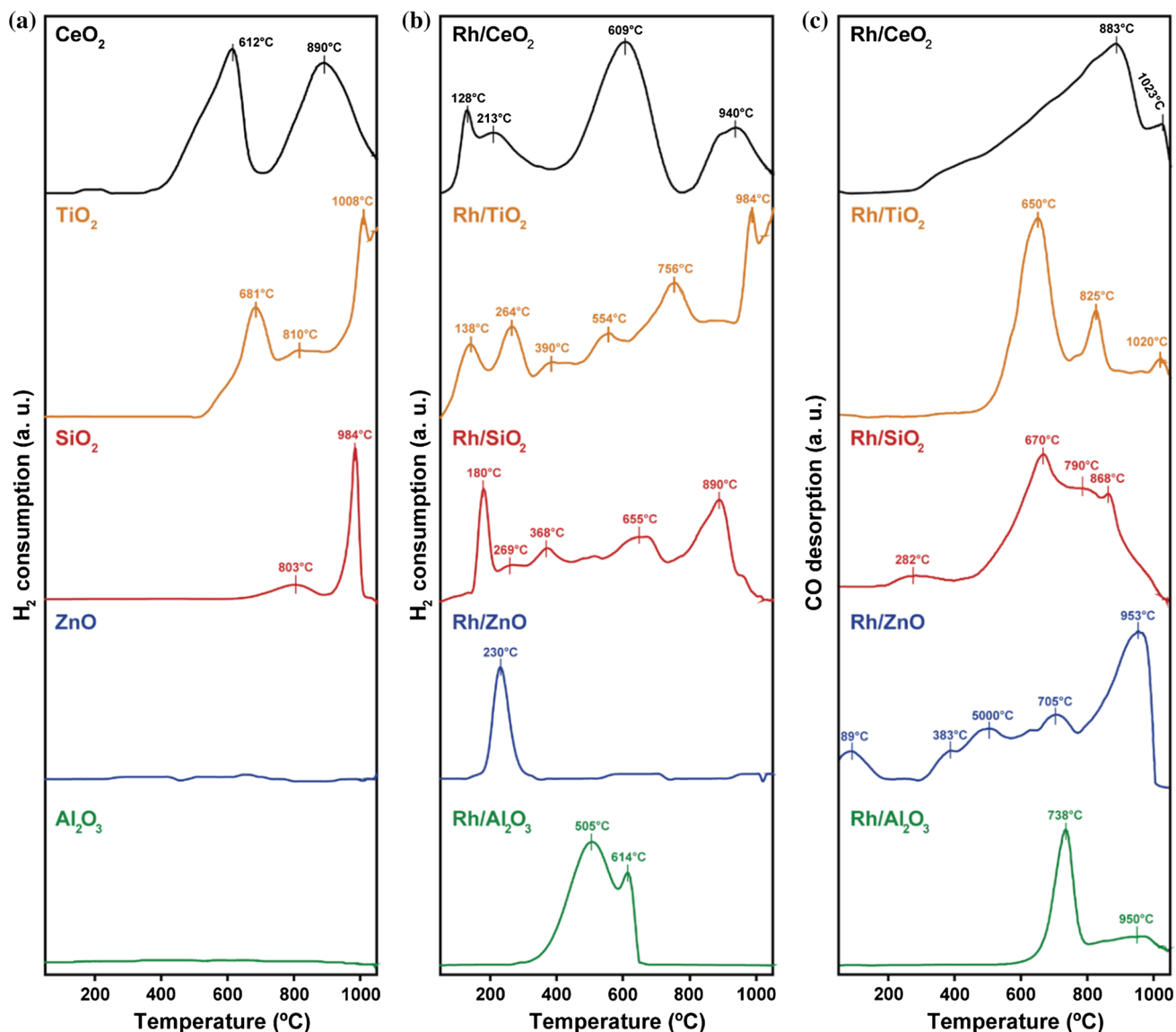
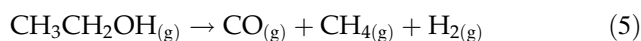
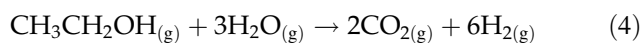


Figure 4 H₂-TPR profiles for the pure commercial oxide supports (a) and Rh/M_xO_y catalysts (b), and CO-TPD profiles for the Rh/M_xO_y catalysts (c).

is considered as the best condition in terms of both ethanol conversion and H₂ selectivity [20, 66, 67].

Herein, pure commercial oxides were also tested for comparison and the results are depicted in Figure S4. Among the pure commercial oxide supports (Figure S4), in terms of ethanol conversion, the catalytic performances decreased in the following order: Al₂O₃ > SiO₂ > ZnO > TiO₂ > CeO₂. However, after addition of Rh and thus the formation of the Rh-based catalysts (Fig. 5), the tendency was completely changed and corresponded to: Rh/CeO₂ = Rh/TiO₂ > Rh/SiO₂ > Rh/ZnO > Rh/Al₂O₃. Interestingly, as well as ethanol conversion, selectivity/product

distribution showed a strong dependence on the nature of the catalyst support. More specifically, in the presence of Rh/CeO₂ (Fig. 5b) and Rh/TiO₂ (Fig. 5c), H₂ and CO₂ were detected as products derived from ethanol steam reforming (Eq. 4) with the formation of CO and low amounts of CH₄ as by-products (Eq. 5).



Even though both catalysts were stable with the complete ethanol conversion at 550 °C over the entire period of 24 h of reaction, the best result can be

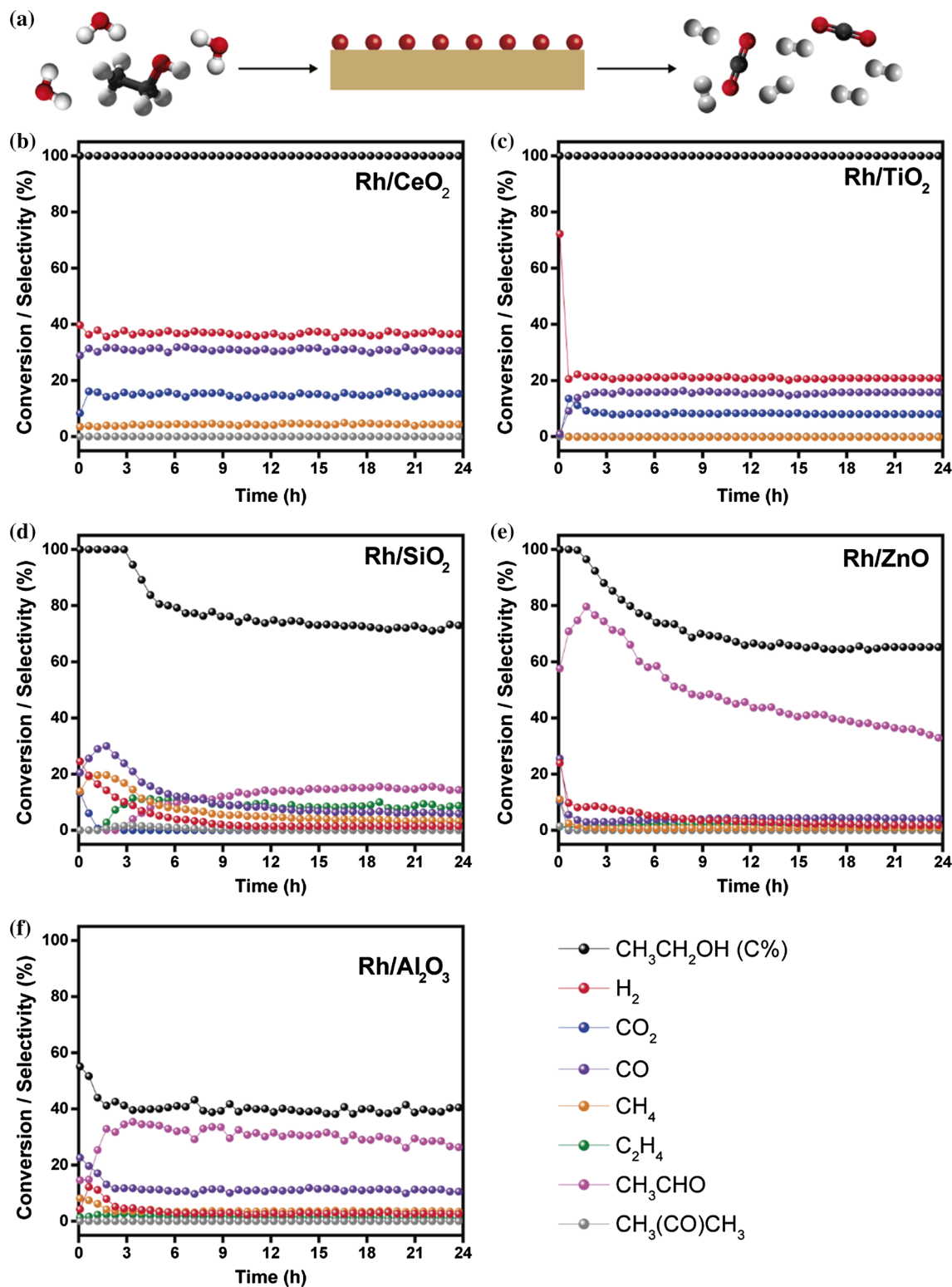
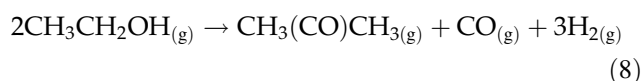
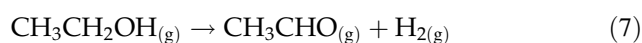
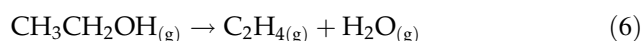


Figure 5 a Scheme for ethanol steam reforming employing Rh/ M_xO_y as catalysts. Ethanol conversion and product selectivities obtained in the presence of b 100 mg of Rh/CeO₂, c 150 mg of

Rh/TiO₂, d 20 mg of Rh/SiO₂, e 10 mg of Rh/ZnO, and f 206 mg of Rh/Al₂O₃ catalysts. The experiments were performed at 550 °C and $\text{H}_2\text{O}/\text{CH}_3\text{CH}_2\text{OH}$ molar ratio = 3.

considered those obtained over Rh/CeO₂ catalyst, in which almost 40% of H₂ selectivity was observed, in contrast to Rh/TiO₂ that presented only 20% of selectivity for this product. This behavior agrees with previous reports, which show that CeO₂ is one of the best supports for improving the ethanol steam reforming reaction, not only for prevention against carbon deposition/deactivation but also for enhancing the formation of H₂ [28, 36, 51, 68, 69]. In this case, it is well established that CeO₂ shows a great oxygen storage capability and oxygen mobility at its surface due to the presence of Ce³⁺ and Ce⁴⁺ ions, which are associated with the prevention against deposition of carbon compounds and the enhancement of catalytic reactions. [28, 51, 68, 69] When Rh/SiO₂ (Fig. 5d) was employed as catalyst, a drop in the ethanol conversion to below 80% was observed after 3 h of reaction and a more complex reaction mixture was observed. In this experiment, other products such as ethene (C₂H₄), acetaldehyde (CH₃CHO), and traces of acetone (CH₃(CO)CH₃) were formed, as described by Eqs. 6–8:



This behavior can be attributed to the neutral and slightly reactive character of SiO₂, which allows the active phases of Rh to catalyze a variety of parallel reactions leading to the formation of several reaction products [70]. On the other hand, in the presence of Rh/ZnO (Fig. 5e) and Rh/Al₂O₃ (Fig. 5f), the dominant reaction in the processes was the ethanol dehydrogenation leading to the formation of acetaldehyde (Eq. 6), which tends to occur preferentially to the steam reforming of ethanol in supports such as ZnO and Al₂O₃, as also observed in previous works [8, 70, 71]. Interestingly, when pure commercial supports were employed as catalyst (Figure S4), even presenting relatively high values for ethanol conversion at 550 °C over the entire period of 24 h of reaction, low values for H₂ production were observed in all cases, illustrating the need of Rh to put forward the ethanol steam reforming process (Eq. 4). Instead of the steam reforming of ethanol, the main products observed were ethylene and acetaldehyde, which are derived from the ethanol dehydration (Eq. 6) and

dehydrogenation (Eq. 7), respectively. More specifically, for solids with basic and slightly acidic characters such as TiO₂, SiO₂, and ZnO, the main reaction was the dehydrogenation of ethanol. However, in the presence of Al₂O₃, an oxide of recognized acidic properties, the dehydration of ethanol was the most favored reaction, according to the literature [8, 24, 70]. In summary, we can point that the catalytic activity, selectivity, and stability were strongly affected by the nature of the oxide support, due to their significant and remarkable differences in their oxygen storage, oxygen mobility, and acidity/basicity.

After the catalytic experiments, all Rh/M_xO_y catalysts were then characterized by XRD (Figure S5, first column), TGA (Figure S5, second column), SEM (Fig. 6), and HRTEM (Fig. 6). The XRD analyses indicated the presence of well-defined peaks assigned to their respective oxide supports suggesting that the overall structures of all Rh/M_xO_y catalysts remained unchanged after the catalytic experiments. Here, Rh/CeO₂ (Figure S5A), Rh/SiO₂ (Figure S5G), and Rh/ZnO (Figure S5J) showed diffraction peaks associated with SiC, which was employed as a diluent in catalytic experiments with these catalysts. For the specific case of Rh/SiO₂ (Figure S5G), only peaks associated with SiC were observed due to its superior crystallinity compared to our commercial SiO₂ [72], which was partially crystalline with the presence of α-cristobalite and tridymite phases. For the experiments using Rh/TiO₂ (Figure S5D) Rh/Al₂O₃ and (Figure S5M) catalysts, as no SiC was demanded, only peaks associated with TiO₂ and Al₂O₃ were observed.

TGA analyzes were also performed to investigate the formation of solid carbon-based structures, which are possible to be formed in the presence of Rh catalysts supported over oxides. Herein, some probable reactions can be pointed as the sources of the formation of carbon structures: decomposition of methane (Eq. 9) and polymerization of ethene (Eq. 10), acetaldehyde (Eq. 11), and acetone (Eq. 12) as follows [21, 22].

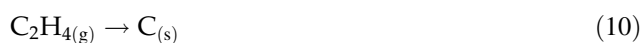
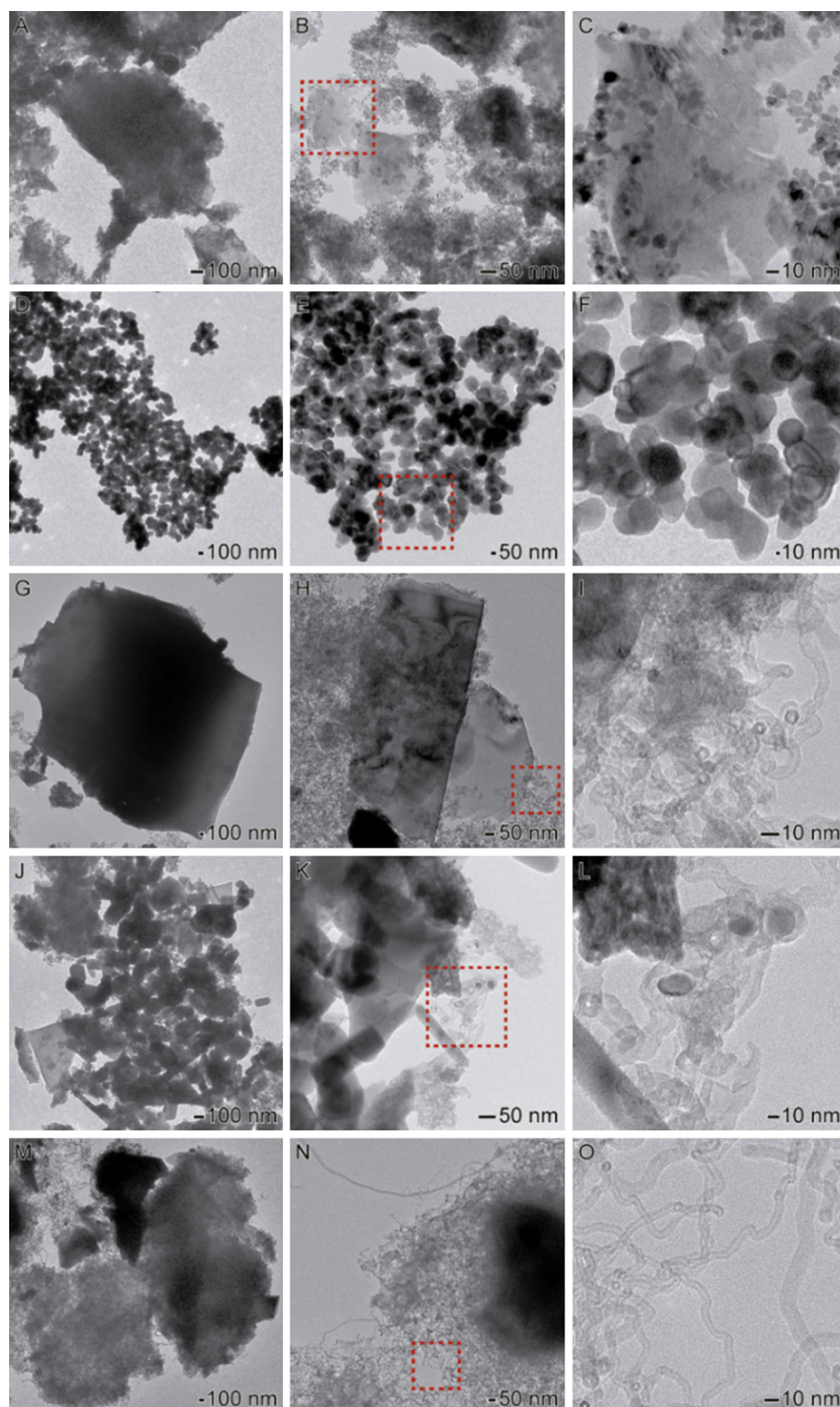


Figure 6 HRTEM images for the Rh/ M_xO_y catalysts after the ethanol steam reforming experiments. **a–c** Rh/CeO₂, **d–f** Rh/TiO₂, **g–i** Rh/SiO₂, **j–l** Rh/ZnO, and **m–o** Rh/Al₂O₃ catalysts.



In the TGA analysis for the Rh/CeO₂ (Figure S5B) and Rh/TiO₂ (Figure S5E), low and no significant

weight loss was observed after heating up to 1000 °C, indicating the low deposition of carbon structures over their surfaces, which is in agreement with the catalytic experiments that showed their stabilities

during all reaction period. Interestingly, the TGA profile for Rh/ZnO (Figure S5K) also suggested the low deposition of carbon structures (0.19%). However, a deactivation process after only 2 h of reaction was observed, which can be associated with the selective carbon deposition over the Rh nanoparticles and chemisorption of poisoning compounds such as CO. In contrast, Rh/SiO₂ (Figure S5H) and Rh/Al₂O₃ (Figure S5N) presented total weight loss of 4.50 and 2.06%, respectively, which justifies their deactivation during the catalytic experiments [73, 74]. For comparison, XRD patterns (left column) and TGA profiles (right column) for the pure commercial oxide supports after the ethanol steam reforming experiments are depicted in Figure S6.

Thus, to identify the type of the formed carbon-based structures during the ethanol steam reforming, we performed HRTEM analyses of the Rh/M_xO_y catalysts after their catalytic studies (Fig. 6). Firstly, we can highlight that all Rh/M_xO_y catalysts presented good stabilities against aggregation under the experimental conditions and no morphological changes could be detected in the samples compared with the fresh catalysts (Fig. 2) in agreement with the XRD results. Such fact indicates the promising application of these materials as catalysts for gas-phase catalytic transformations. Interestingly, we could also observe the formation of carbon-based nanostructures and identify their morphologies in the presence of each employed catalyst. More specifically, after the catalytic ethanol steam reforming in the presence of Rh/CeO₂ (Fig. 6b, c), carbon-based nanosheets could be detected, even in low amounts, in agreement with the TGA profile, which showed a weight loss of only 0.24% up to 1000 °C. On the other hand, in the presence of Rh/TiO₂ (Fig. 6e, f), no carbon structures could be detected, which also agree with the TGA result. In the presence of Rh/SiO₂ (Fig. 6h, i), Rh/ZnO (Fig. 6k, l), and Rh/Al₂O₃ (Fig. 6n, o), the formation of carbon nanotubes and carbon onions was observed. Herein, the amount of carbon-based structures also accompanied the tendency indicated in the TGA analyses and decreased as follows: Rh/SiO₂ > Rh/Al₂O₃ > Rh/ZnO.

Interestingly, the catalytic results agreed with the TGA and HRTEM results for the catalyst after the catalytic experiments. In this case, the catalysts that presented lower carbon deposition (Rh/CeO₂ and Rh/TiO₂) showed superior stabilities toward ethanol steam reforming. And Rh/Al₂O₃ and Rh/SiO₂, which

presented superior values of weight loss, presented lower values of ethanol conversion and deactivation profiles. The exception to this tendency is Rh/ZnO, which showed only 0.19% of weight loss but, even in low amount, the deposited carbon structures led to the catalyst deactivation.

Conclusions

In summary, we have demonstrated the synthesis of Rh-supported catalysts, which can be described by Rh nanoparticles anchored over the surface of a variety of commercial inorganic oxides that include CeO₂, TiO₂, SiO₂, ZnO, and Al₂O₃. To this end, a single-step approach based on the reduction and further deposition of Rh³⁺ to Rh was successfully employed using urea and mediator in the absence of any other stabilizer or capping agent. Interestingly, the obtained catalysts were relatively similar in terms of nanoparticle size distribution, shape, and surface distribution, differing only in terms of the nature of support. Herein, their properties were strongly dependent on the nature of the support as well as their catalytic behavior toward ethanol steam reforming, which decreased in the following order: Rh/CeO₂ = Rh/TiO₂ > Rh/SiO₂ > Rh/ZnO > Rh/Al₂O₃ in terms of ethanol conversion. On the other hand, their selectivities and stabilities were also strongly influenced by the nature of the catalytic support. More specifically, in the presence of different supports, four main reaction paths could be observed: (1) ethanol steam reforming (Rh/CeO₂ and Rh/TiO₂), (2) ethanol dehydration (Rh/SiO₂), (3) ethanol decomposition (Rh/CeO₂ and Rh/SiO₂), and (4) ethanol dehydrogenation (Rh/SiO₂, Rh/ZnO, and Rh/Al₂O₃). In terms of stability, their deactivation profiles were also affected by nature of the support, in which the reactions with superior deposition of carbon-based compounds led to faster deactivation. Thus, our results suggested that the correct choice of the support for the synthesis of heterogeneous nanocatalysts is a key element to prepared nanomaterials with enhanced catalytic performances. We believe that our reported results may represent an important contribution in the synthesis of Rh-supported catalysts for gas-phase transformations such as the ethanol steam reforming reaction.

Acknowledgements

This work was supported by FAPESP (Grant Nos. 2014/09087-4, 2014/50279-4, and 2015/26308-7). F.C.F, M.L., and P.H.C.C. thank the CNPq for their research fellowships. T.S.R. (scholarship 2017/04929-5) and A.G.M.S. thank FAPESP for their fellowships. E.G.C. and F.A.S. thank CNPq for their fellowships. R.S.G. thanks CAPES for his fellowship.

Compliance with ethical standards

Conflict of interest The authors declare that they have no conflict of interest. P.H.C. Camargo is an editor of this journal. He was not involved in any aspect of the review process and not permitted to see any information about the review process on the editorial management system.

Electronic supplementary material: The online version of this article (<https://doi.org/10.1007/s10853-019-03660-z>) contains supplementary material, which is available to authorized users.

References

- Haryanto A, Fernando S, Murali N, Adhikari S (2005) Current status of hydrogen production techniques by steam reforming of ethanol: a review. *Energy Fuels* 19:2098–2106. <https://doi.org/10.1021/ef0500538>
- Ni M, Leung DY, Leung MKH (2007) A review on reforming bio-ethanol for hydrogen production. *Int J Hydrog Energy* 32:3238–3247. <https://doi.org/10.1016/j.ijhydene.2007.04.038>
- Moretti E, Storaro L, Talon A et al (2015) Ceria–zirconia based catalysts for ethanol steam reforming. *Fuel* 153:166–175. <https://doi.org/10.1016/j.fuel.2015.02.077>
- Vaidya PD, Wu Y-J, Rodrigues AE (2019) Chapter 13: Kinetics of ethanol steam reforming for hydrogen production. In: Basile A, Iulianelli A, Dalena F, Veziroğlu TNBT-E (eds) *Ethanol science and engineering*. Elsevier, pp 341–354
- Sharma YC, Kumar A, Prasad R, Upadhyay SN (2017) Ethanol steam reforming for hydrogen production: latest and effective catalyst modification strategies to minimize carbonaceous deactivation. *Renew Sustain Energy Rev* 74:89–103. <https://doi.org/10.1016/j.rser.2017.02.049>
- Pinton N, Vidal MV, Signoretto M et al (2017) Ethanol steam reforming on nanostructured catalysts of Ni, Co and CeO₂: influence of synthesis method on activity, deactivation and regenerability. *Catal Today* 296:135–143. <https://doi.org/10.1016/j.cattod.2017.06.022>
- Contreras JL, Salmones J, Colin-Luna JA et al (2014) Catalysts for H₂ production using the ethanol steam reforming (a review). *Int J Hydrog Energy* 39:18835–18853. <https://doi.org/10.1016/j.ijhydene.2014.08.072>
- Llorca J, Homs N, Sales J, de la Piscina PR (2002) Efficient production of hydrogen over supported cobalt catalysts from ethanol steam reforming. *J Catal* 209:306–317. <https://doi.org/10.1006/jcat.2002.3643>
- Riani P, Garbarino G, Lucchini MA et al (2014) Unsupported versus alumina-supported Ni nanoparticles as catalysts for steam/ethanol conversion and CO₂ methanation. *J Mol Catal A Chem* 383–384:10–16. <https://doi.org/10.1016/j.molcata.2013.11.006>
- Varga E, Pusztai P, Ovari L et al (2015) Probing the interaction of Rh, Co and bimetallic Rh–Co nanoparticles with the CeO₂ support: catalytic materials for alternative energy generation. *Phys Chem Chem Phys* 17:27154–27166. <https://doi.org/10.1039/C5CP03549J>
- Coronel L, Múnera JF, Tarditi AM et al (2014) Hydrogen production by ethanol steam reforming over Rh nanoparticles supported on lanthana/silica systems. *Appl Catal B Environ* 160:254–266. <https://doi.org/10.1016/j.apcatb.2014.05.025>
- Li T, Zhang J, Xie X et al (2015) Montmorillonite-supported Ni nanoparticles for efficient hydrogen production from ethanol steam reforming. *Fuel* 143:55–62. <https://doi.org/10.1016/j.fuel.2014.11.033>
- Moraes TS, Neto RCR, Ribeiro MC et al (2015) Effects of ceria morphology on catalytic performance of Ni/CeO₂ catalysts for low temperature steam reforming of ethanol. *Top Catal* 58:281–294. <https://doi.org/10.1007/s11244-015-0369-x>
- Vargas JC, Ivanova S, Thomas S et al (2012) Influence of gold on Ce–Zr–Co fluorite-type mixed oxide catalysts for ethanol steam reforming. *Catalysts* 2:121–138
- Lim H, Gu Y, Oyama ST (2012) Studies of the effect of pressure and hydrogen permeance on the ethanol steam reforming reaction with palladium- and silica-based membranes. *J Membr Sci* 396:119–127. <https://doi.org/10.1016/j.memsci.2012.01.004>
- Kourtelesis M, Panagiotopoulou P, Verykios XE (2015) Influence of structural parameters on the reaction of low temperature ethanol steam reforming over Pt/Al₂O₃ catalysts. *Catal Today* 258:247–255. <https://doi.org/10.1016/j.cattod.2014.12.035>
- Remiro A, Ochoa A, Arandia A et al (2019) On the dynamics and reversibility of the deactivation of a Rh/CeO₂ZrO₂ catalyst in raw bio-oil steam reforming. *Int J*

- Hydrog Energy 44:2620–2632. <https://doi.org/10.1016/j.ijhydene.2018.12.073>
- [18] Moraes TS, Borges LEP, Farrauto R, Noronha FB (2018) Steam reforming of ethanol on Rh/SiCeO₂ washcoated monolith catalyst: stable catalyst performance. *Int J Hydrog Energy* 43:115–126. <https://doi.org/10.1016/j.ijhydene.2017.10.180>
- [19] Bosko ML, Ferreira N, Catena A et al (2018) Catalytic behavior of Ru nanoparticles supported on carbon fibers for the ethanol steam reforming reaction. *Catal Commun* 114:19–23. <https://doi.org/10.1016/j.catcom.2018.05.019>
- [20] Augusto BL, Noronha FB, Fonseca FC et al (2014) Nickel/gadolinium-doped ceria anode for direct ethanol solid oxide fuel cell. *Int J Hydrog Energy* 39:11196–11209. <https://doi.org/10.1016/j.ijhydene.2014.05.088>
- [21] Fajardo H, Longo E, Mezalira D et al (2010) Influence of support on catalytic behavior of nickel catalysts in the steam reforming of ethanol for hydrogen production. *Environ Chem Lett* 8:79–85. <https://doi.org/10.1007/s10311-008-0195-5>
- [22] Lovón ASP, Lovón-Quintana JJ, Almerindo GI et al (2012) Preparation, structural characterization and catalytic properties of Co/CeO₂ catalysts for the steam reforming of ethanol and hydrogen production. *J Power Sources*. <https://doi.org/10.1016/j.jpowsour.2012.05.066>
- [23] Soykal II, Sohn H, Ozkan US (2012) Effect of support particle size in steam reforming of ethanol over Co/CeO₂ catalysts. *ACS Catal* 2:2335–2348. <https://doi.org/10.1021/cs3004159>
- [24] Moura JS, Souza MOG, Bellido JDA et al (2012) Ethanol steam reforming over rhodium and cobalt-based catalysts: effect of the support. *Int J Hydrog Energy* 37:3213–3224. <https://doi.org/10.1016/j.ijhydene.2011.10.112>
- [25] Choong KKS, Chen L, Du Y et al (2017) The role of metal–support interaction for CO-free hydrogen from low temperature ethanol steam reforming on Rh–Fe catalysts. *Phys Chem Chem Phys* 19:4199–4207. <https://doi.org/10.1039/C6CP05934A>
- [26] Rodrigues TS, da Silva AGM, Gonçalves MC et al (2015) AgPt hollow nanodendrites: synthesis and uniform dispersion over SiO₂ support for catalytic applications. *ChemNanoMat*. <https://doi.org/10.1002/cnma.201500025>
- [27] da Silva AGM, Rodrigues TS, Taguchi LSK et al (2016) Pd-based nanoflowers catalysts: controlling size, composition, and structures for the 4-nitrophenol reduction and BTX oxidation reactions. *J Mater Sci* 51:603–614. <https://doi.org/10.1007/s10853-015-9315-3>
- [28] Rodrigues TS, da Silva AHM, da Silva AGM et al (2016) Hollow AgPt/SiO₂ nanomaterials with controlled surface morphologies: is the number of Pt surface atoms imperative to optimize catalytic performances? *Catal Sci Technol* 6:2162–2170. <https://doi.org/10.1039/C5CY01415H>
- [29] Rodrigues TS, Da Silva AGM, Gonçalves MC et al (2016) Catalytic properties of AgPt nanoshells as a function of size: larger outer diameters lead to improved performances. *Langmuir* 32:9371–9379. <https://doi.org/10.1021/acs.langmuir.6b01783>
- [30] Kisukuri CM, Palmeira DJ, Rodrigues TS et al (2016) Bimetallic nanoshells as platforms for metallo- and biometallo-catalytic applications. *ChemCatChem* 8:171–179. <https://doi.org/10.1002/cctc.201500812>
- [31] da Silva AGM, Rodrigues TS, Haigh SJ, Camargo PHC (2017) Galvanic replacement reaction: recent developments for engineering metal nanostructures towards catalytic applications. *Chem Commun* 53:7135–7148. <https://doi.org/10.1039/C7CC02352A>
- [32] Gu D, Tseng JC, Weidenthaler C et al (2016) Gold on different manganese oxides: ultra-low-temperature CO oxidation over colloidal gold supported on bulk-MnO₂ nanomaterials. *J Am Chem Soc* 138:9572–9580. <https://doi.org/10.1021/jacs.6b04251>
- [33] da Silva AGM, Kisukuri CM, Rodrigues TS et al (2016) MnO₂ nanowires decorated with Au ultrasmall nanoparticles for the green oxidation of silanes and hydrogen production under ultralow loadings. *Appl Catal B Environ* 184:35–43. <https://doi.org/10.1016/j.apcatb.2015.11.023>
- [34] Zanella R, Giorgio S, Henry CR, Louis C (2002) Alternative methods for the preparation of gold nanoparticles supported on TiO₂. *J Phys Chem B* 106:7634–7642. <https://doi.org/10.1021/jp0144810>
- [35] Yentekakis IV, Goula G, Kampouri S et al (2018) Ir-catalysed nitrous oxide (N₂O) decomposition: effect of ir particle size and metal–support interactions. *Catal Lett* 148:341–347. <https://doi.org/10.1007/s10562-017-2233-z>
- [36] Yentekakis IV, Goula G, Hatzisymeon M et al (2019) Effect of support oxygen storage capacity on the catalytic performance of Rh nanoparticles for CO₂ reforming of methane. *Appl Catal B Environ* 243:490–501. <https://doi.org/10.1016/j.apcatb.2018.10.048>
- [37] Yang N, Bent SF (2017) Investigation of inherent differences between oxide supports in heterogeneous catalysis in the absence of structural variations. *J Catal* 351:49–58. <https://doi.org/10.1016/j.jcat.2017.04.003>
- [38] Palma V, Castaldo F, Ciambelli P, Iaquaniello G (2014) CeO₂-supported Pt/Ni catalyst for the renewable and clean H₂ production via ethanol steam reforming. *Appl Catal B Environ* 145:73–84. <https://doi.org/10.1016/j.apcatb.2013.01.053>
- [39] Yoo JB, Kim HS, Kang SH et al (2014) Hollow nickel-coated silica microspheres containing rhodium nanoparticles

- for highly selective production of hydrogen from hydrous hydrazine. *J Mater Chem A* 2:18929–18937. <https://doi.org/10.1039/C4TA03550J>
- [40] da Silva AGM, Batalha DC, Rodrigues TS et al (2018) Sub-15 nm CeO₂ nanowires as an efficient non-noble metal catalyst in the room-temperature oxidation of aniline. *Catal Sci Technol* 8:1828–1839. <https://doi.org/10.1039/C7CY02402A>
- [41] Wu Z, Li M, Howe J et al (2010) Probing defect sites on CeO₂ nanocrystals with well-defined surface planes by Raman spectroscopy and O₂ adsorption. *Langmuir* 26:16595–16606. <https://doi.org/10.1021/la101723w>
- [42] Frost RL, Kristof J, Rintoul L, Klopogge JT (2000) Raman spectroscopy of urea and urea-intercalated kaolinites at 77 K. *Spectrochim Acta Part A Mol Biomol Spectrosc* 56:1681–1691. [https://doi.org/10.1016/S1386-1425\(00\)00223-7](https://doi.org/10.1016/S1386-1425(00)00223-7)
- [43] Wang Y, Peng X, Shi J et al (2012) Highly selective fluorescent chemosensor for Zn²⁺ derived from inorganic–organic hybrid magnetic core/shell Fe₃O₄@SiO₂ nanoparticles. *Nanoscale Res Lett* 7:86. <https://doi.org/10.1186/1556-276X-7-86>
- [44] Karunakaran C, Anilkumar P, Gomathisankar P (2011) Photoproduction of iodine with nanoparticulate semiconductors and insulators. *Chem Cent J* 5:31. <https://doi.org/10.1186/1752-153X-5-31>
- [45] Hussain M, Ahmad M, Nisar A et al (2014) Enhanced photocatalytic and electrochemical properties of Au nanoparticles supported TiO₂ microspheres. *New J Chem* 38:1424–1432. <https://doi.org/10.1039/C3NJ01525D>
- [46] da Silva AGM, Rodrigues TS, Candido EG et al (2018) Combining active phase and support optimization in MnO₂-Au nanoflowers: enabling high activities towards green oxidations. *J Colloid Interface Sci* 530:282–291. <https://doi.org/10.1016/j.jcis.2018.06.089>
- [47] Haruta M (1997) Novel catalysis of gold deposited on metal oxides. *Catal Surv Asia* 1:61–73. <https://doi.org/10.1023/A:1019068728295>
- [48] Patil NS, Uphade BS, McCulloh DG et al (2004) Styrene epoxidation over gold supported on different transition metal oxides prepared by homogeneous deposition–precipitation. *Catal Commun* 5:681–685. <https://doi.org/10.1016/j.catcom.2004.08.006>
- [49] Diaz E, Mohedano AF, Casas JA et al (2016) On the performance of Pd and Rh catalysts over different supports in the hydrodechlorination of the MCPA herbicide. *Appl Catal B Environ* 186:151–156. <https://doi.org/10.1016/j.apcatb.2015.12.054>
- [50] Pal P, Pahari SK, Sinhamahapatra A et al (2013) CeO₂ nanowires with high aspect ratio and excellent catalytic activity for selective oxidation of styrene by molecular oxygen. *RSC Adv* 3:10837–10847. <https://doi.org/10.1039/C3RA23485A>
- [51] Silva AGM, Rodrigues TS, Dias A et al (2014) Ce_{1-x}Sm_xO_{1.9}-[small delta] nanoparticles obtained by microwave-assisted hydrothermal processing: an efficient application for catalytic oxidation of [small alpha]-bisabolol. *Catal Sci Technol* 4:814–821. <https://doi.org/10.1039/C3CY00788J>
- [52] Córdoba G, Viniegra M, Fierro JLG et al (1998) TPR, ESR, and XPS Study of Cu²⁺ ions in sol–gel-derived TiO₂. *J Solid State Chem* 138:1–6. <https://doi.org/10.1006/jssc.1997.7690>
- [53] Gualteros JAD, Garcia MAS, da Silva AGM et al (2019) Synthesis of highly dispersed gold nanoparticles on Al₂O₃, SiO₂, and TiO₂ for the solvent-free oxidation of benzyl alcohol under low metal loadings. *J Mater Sci* 54:238–251. <https://doi.org/10.1007/s10853-018-2827-x>
- [54] Gao Q, Xu B, Tong Q, Fan Y (2016) Selective hydrogenolysis of raw glycerol to 1,2-propanediol over Cu–ZnO catalysts in fixed-bed reactor. *Biosci Biotechnol Biochem* 80:215–220. <https://doi.org/10.1080/09168451.2015.1088372>
- [55] Deng T, Liu H (2013) Promoting effect of SnO_x on selective conversion of cellulose to polyols over bimetallic Pt–SnO_x/Al₂O₃ catalysts. *Green Chem* 15:116–124. <https://doi.org/10.1039/C2GC36088H>
- [56] Gac W, Zawadzki W, Słowik G et al (2016) Chromium-modified zinc oxides. *J Therm Anal Calorim* 125:1205–1215. <https://doi.org/10.1007/s10973-016-5586-4>
- [57] da Silva AHM, Rodrigues TS, da Silva AGM et al (2017) Systematic investigation of the effect of oxygen mobility on CO oxidation over AgPt nanoshells supported on CeO₂, TiO₂ and Al₂O₃. *J Mater Sci* 52:13764–13778. <https://doi.org/10.1007/s10853-017-1481-z>
- [58] Huang C, Ma Z, Miao C et al (2017) Catalytic decomposition of N₂O over Rh/Zn–Al₂O₃ catalysts. *RSC Adv* 7:4243–4252. <https://doi.org/10.1039/C6RA25388A>
- [59] Wang C, Zheng T, Lu J et al (2017) Three-way catalytic reactions on Rh-based catalyst: effect of Rh/ceria interfaces. *Appl Catal A Gen* 544:30–39. <https://doi.org/10.1016/j.apcata.2017.07.003>
- [60] Chen G, Guo C-Y, Huang Z, Yuan G (2011) Synthesis of ethanol from syngas over iron-promoted Rh immobilized on modified SBA-15 molecular sieve: effect of iron loading. *Chem Eng Res Des* 89:249–253. <https://doi.org/10.1016/j.cherd.2010.07.014>
- [61] Li F, Qian W (2017) Effect of Fe impregnation sequence on ethanol synthesis from syngas over Mn and Fe promoted Rh/γ-Al₂O₃. *Appl Petrochem Res* 7:161–167. <https://doi.org/10.1007/s13203-017-0189-y>

- [62] Steil MC, Nobrega SD, Georges S et al (2017) Durable direct ethanol anode-supported solid oxide fuel cell. *Appl Energy* 199:180–186. <https://doi.org/10.1016/j.apenergy.2017.04.086>
- [63] Klouz V, Fierro V, Denton P et al (2002) Ethanol reforming for hydrogen production in a hybrid electric vehicle: process optimisation. *J Power Sources* 105:26–34. [https://doi.org/10.1016/S0378-7753\(01\)00922-3](https://doi.org/10.1016/S0378-7753(01)00922-3)
- [64] Mattos LV, Jacobs G, Davis BH, Noronha FB (2012) Production of hydrogen from ethanol: review of reaction mechanism and catalyst deactivation. *Chem Rev* 112:4094–4123. <https://doi.org/10.1021/cr2000114>
- [65] Karim AM, Su Y, Sun J et al (2010) A comparative study between Co and Rh for steam reforming of ethanol. *Appl Catal B Environ* 96:441–448. <https://doi.org/10.1016/j.apcatalb.2010.02.041>
- [66] da Silva AAA, Bion N, Epron F et al (2017) Effect of the type of ceria dopant on the performance of Ni/CeO₂ SOFC anode for ethanol internal reforming. *Appl Catal B Environ* 206:626–641. <https://doi.org/10.1016/j.apcatalb.2017.01.069>
- [67] Nobrega SD, Gelin P, Georges S et al (2014) A fuel-flexible solid oxide fuel cell operating in gradual internal reforming. *J Electrochem Soc* 161:F354–F359. <https://doi.org/10.1149/2.107403jes>
- [68] Gupta A, Waghmare UV, Hegde MS (2010) Correlation of oxygen storage capacity and structural distortion in transition-metal-, noble-metal-, and rare-earth-ion-substituted CeO₂ from first principles calculation. *Chem Mater* 22:5184–5198. <https://doi.org/10.1021/cm101145d>
- [69] Kehoe AB, Scanlon DO, Watson GW (2011) Role of lattice distortions in the oxygen storage capacity of divalently doped CeO₂. *Chem Mater* 23:4464–4468. <https://doi.org/10.1021/cm201617d>
- [70] Batista MS, Santos RKS, Assaf EM et al (2003) Characterization of the activity and stability of supported cobalt catalysts for the steam reforming of ethanol. *J Power Sources* 124:99–103. [https://doi.org/10.1016/S0378-7753\(03\)00599-8](https://doi.org/10.1016/S0378-7753(03)00599-8)
- [71] Ferencz Z, Erdőhelyi A, Baán K et al (2014) Effects of support and Rh additive on Co-based catalysts in the ethanol steam reforming reaction. *ACS Catal* 4:1205–1218. <https://doi.org/10.1021/cs500045z>
- [72] Dhiman R, Johnson E, Skou EM et al (2013) SiC nanocrystals as Pt catalyst supports for fuel cell applications. *J Mater Chem A* 1:6030–6036. <https://doi.org/10.1039/C3TA10238F>
- [73] Calles AJ, Carrero A, Vizcaino JA, Lindo M (2015) Effect of Ce and Zr addition to Ni/SiO₂ catalysts for hydrogen production through ethanol steam reforming. *Catalysts* 5:58–76. <https://doi.org/10.3390/catal5010058>
- [74] Cavallaro S, Mondello N, Freni S (2001) Hydrogen produced from ethanol for internal reforming molten carbonate fuel cell. *J Power Sources* 102:198–204. [https://doi.org/10.1016/S0378-7753\(01\)00800-X](https://doi.org/10.1016/S0378-7753(01)00800-X)

Publisher's Note Springer Nature remains neutral with regard to jurisdictional claims in published maps and institutional affiliations.